Using X-ray computed tomography in pore structure characterization for a Berea sandstone: Resolution effect

Sheng Peng [a,*], Qinhong Hu [a,*], Stefan Dultz [b], Ming Zhang [c]

[a] Department of Earth and Environmental Sciences, University of Texas at Arlington, Arlington, TX 76019, USA
[b] Institute for Mineralogy, Leibniz University Hannover, Callinstr. 3, D-30167 Hannover, Germany
[c] Institute for Geo-Resources and Environment, National Institute of Advanced Industrial Science and Technology (AIST), Onogawa 16-1, Tsukuba, Ibaraki 305-8569, Japan

SUMMARY

X-ray computed tomography (XCT) is a powerful tool for detecting the micro-scale pore structure and has been applied to many natural and synthetic porous media. However, due to the resolution limitations, either non-representative view of the sample or inaccurate results can be produced from the XCT image processing. In this paper, two XCT (micro-CT and CT with synchrotron radiation) with different resolutions of 12.7 μm and 0.35 μm, as well as mercury intrusion porosimetry (MIP) with a minimum detection limit of 3 nm, were used for Berea sandstone to investigate the effect of detecting resolution on the pore structure. Several key pore structure parameters, including porosity, pore size distribution, pore connectivity, surface area, hydraulic radius, and aspect ratio were analyzed in a manner of quantitative comparison between different resolutions of XCT and MIP. The low resolution XCT can capture the large-pore porosity, while overestimates the pore size and pore connectivity. The high resolution XCT is more accurate in describing the pore shape, porosity, pore size; however, it is not representative since narrower detecting pore size range and small volume represented. A representative element volume related to large-pore porosity and probably large-pore connectivity with diameter and height of 2.8 mm is obtained through scale effect analysis. Therefore, selecting an appropriate resolution should be a compromise between the pore size and the representative element volume for the specific property or process of interest.

© 2012 Elsevier B.V. All rights reserved.

1. Introduction

The internal micro-scale pore structure of natural rock has been of interest to researchers for decades since it can provide information on pore geometry and topology, two determining factors related to many hydraulic/transport properties of a rock, such as permeability and diffusivity. In addition, pore structure mapping directly from the real sample can provide the physical framework for pore-scale network models (Bryant et al., 1993; Bhattad et al., 2010), in which pore geometry and topology are incorporated explicitly, therefore no adjustable parameters, such as porosity, tortuosity, and relative permeability, are required for single- or multi-phase flow simulations (e.g., Blunt et al., 1992; Hilpert et al., 2000; Gladkikh and Bryant, 2005). Many efforts have been used to quantitatively characterize pore structure with different methods, which can be classified as direct imaging methods and various indirect methods as described by Amirtharaj et al. (2011). The direct imaging methods, such as backscatter scanning electron microscopy (Ioannidis et al., 1996), X-ray computed

tomography (XCT) with either conventional or synchrotron radiation (Brusseau et al., 2006; Dong and Blunt, 2009; Fredrich et al., 2006; Wildenschild et al., 2002), and Focus Ion Beam nanotomography (FIB-nt, Bera et al., 2011; Holzer and Cantoni, 2011; Keller et al., 2011), in recent decades have been used to construct the 3D pore structure and phase distributions in pore scale for natural and synthetic porous media.

There is a contradictory feature regarding the spatial resolution and sampling area of the imaging methods. The higher resolution (i.e., clearer image obtained for smaller dimensions) the method can provide, the smaller will be the field of view due to the technical limitation (Dufresne et al., 2004). For example, FIB-nt usually has the resolution of approximately 10 nm, and can generate images for a 3D cube with a dimension of only $\sim$10 μm^3 (e.g., Munchw and Holzer, 2008; Keller et al., 2011). This is valuable for tight rocks with small pores, such as shale, with most of its pores in nm scale. For coarser rocks, however, it will miss the large pores and may not produce representative pore structure information due to the inherent larger-scale heterogeneity. Conversely, methods with a lower resolution, such as XCT, which usually have resolutions larger than 2.1 μm (Bera et al., 2011), can cover a larger sample area and therefore be more representative in terms of pore

* Corresponding authors. Tel.: +1 817 983 4514 (S. Peng).
E-mail addresses: pengsheng2011@gmail.com (S. Peng), maxhu@uta.edu (Q. Hu).

structures, especially for coarse rocks; however, it cannot capture the pore structures smaller than the detecting limit. Therefore, in the application of such imaging techniques, the effect of resolution on the resultant pore structure characterization and subsequent flow analysis has to be considered. However, such resolution effect was missed in many researches and therefore requires further investigation.

Indirect pore geometry/structure probes include gas adsorption/condensation (such as N_2 or water vapor), mercury intrusion porosimetry (MIP), and nuclear magnetic resonance (NMR) relaxometry and imaging (Amirtharaj et al., 2011). Pore surface area, pore size distribution (PSD), and pore connectivity can be deduced from nitrogen adsorption–desorption curves (Barret et al., 1951; Seaton et al., 1989) or mercury intrusion–extrusion curves (Murray et al., 1999). These methods have the ability to cover a wider pore-space range and be more quantitative. For example, MIP can detect the pore diameter from 3 nm to 360 μm (Webb, 2001). Therefore, MIP can serve as a good reference for the XCT-based results. However, the absence of consideration of hysteresis in a simple pore-shape model may cause predictions to differ from real pore-size distributions. For MIP, the PSD can be obtained from the cumulative intrusion pore volume with pore diameter being determined by Washburn's equation (Washburn, 1951). This assumes that the pores are cylindrical, which is different from the more realistic and complicated pore shapes as observed in the imaging methods. Hysteresis occurs as percolation of mercury under each pressure step can only occur if the pores are connected to larger or equal pores. This adds more uncertainty to the indirectly measured PSD, which has been reported to deviate substantially from PSD arising from BSE (Diamond and Leeman, 1995; Ye, 2003).

In this study, XCT methods were employed to investigate the micro-scale pore structure of a Berea sandstone sample. Berea sandstone is one of the principal representatives for typical reservoir rock (e.g., Chen and Song, 2002; Lindquist et al., 1996; Prodanovic et al., 2007). Two resolutions with approximate two-order-magnitude difference were used to investigate the effect of resolution. 3D pore structure was reconstructed based on the 2D XCT images, from which porosity, pore geometry and topology parameters were extracted and discussed. Furthermore, MIP was used for a larger sample and the result is discussed in relation to the resolution obtained with XCT.

2. Materials and methods

2.1. Sample description

The widely-studied Berea sandstone, from the Berea Quarry in Ohio, is an uncemented, homogeneous rock, with a narrow pore-size distribution (Bera et al., 2011). Helium porosity for a cylindrical core sample (2.54 cm i.d., 4 cm height) was measured by Core Laboratories Inc. (Aurora, CO) following standard procedures of API RP 40 (1960). The core sample was placed in a Coberly-Stevens Boyle's Law porosimeter and injected with helium at approximately 100 psig. Corresponding pressures and volumes were measured and utilized in the Boyle's Law equation to calculate sample grain volume. Pore volume was determined by subtracting the grain volume from the measured bulk volume (determined by Archimedes Principle using mercury immersion), and the total porosity was then calculated from the grain and bulk volumes.

2.2. X-ray microtomography

Two X-ray microtomography methods were used for their corresponding high and low resolution in this work: one synchrotron CT in Switzerland, and another micro-CT performed in Japan. The

TOMCAT beamline for X-ray tomographic microscopy at the Swiss light source of the Paul Scherrer Institute in Villigen is optimized for high resolution microtomography. The beamline get photons from a 2.9 T superbend with a critical energy of 11.1 keV making energies above 20 keV accessible (Stampanoni et al., 2006). For stable and homogeneous beam quality, the number of optical elements has been kept to a minimum. For sub-micrometer resolution sample absorption is a critical issue. Thus cylindrical samples as small as possible are needed. For determinations on Berea sandstone a cylindrical specimen 2.1 mm in diameter and a height of 5 mm was sampled from a rock fragment, previously impregnated with an epoxy resin (Araldite), with a corer and mounted with wax on a pin which fits to the sample holder of the instrument. An objective with a magnification of 20× allowing a field of view 0.75×0.75 mm^2 was used. Typically 2,048 images with a pixel size of 0.35 μm were recorded, with the voxel size of $0.35 \times 0.35 \times 0.35$ μm.

The second cylindrical sample of Bera sandstone was 6.5 mm in diameter by 6.5 mm in length. 512 images with a pixel size of 12.7 μm were recorded using an X-ray Microscopic CT Scanner (Microscopic Scan Co., LTD, Japan). The CT scanner used in the study has a capacity for scanning a sample with a maximum dimension up to 50 mm and a resolution of 1 μm. The sample was scanned under the conditions of 100 kV and 0.020 mA. The samples used in the two XCT scanning, along with the samples used in MIP as will be discussed later, were from the same Berea sandstone core.

2.3. XCT data processing

The 2D aerial view images of the rock sample obtained from the XCT were processed with Blob3D, a program designed for processing large three-dimensional data sets, principally those produced by XCT (Ketcham, 2005). A medium smoothing filter was applied with a box radius of 1 to reduce the noise with minimum alteration of the pore geometry. Determining the boundary grayscale threshold is critical for the final results on the pore geometry, and can be carried out by either thresholding algorithms or manually; as indicated in Baveye et al. (2010), in which three CT images were analyzed by 13 experts using different routines. However, no assurance can be provided that any of them are more "correct" than the other. In this work, several thresholding algorithms were tested first; however, obvious improper results were obtained. For example, using Otsu's algorithm (1979), the threshold grayscale for the low resolution and high resolution image is 173 and 255, respectively, corresponding to porosity of ~100%. A minimum-error algorithm (Kittler and Illingworth, 1986), on the other hand, did not converge on these two sets of images. Therefore, operator selected thresholding was used in this study. Ten sample patches were randomly selected for both pore and grain with ImageJ (Abramoff et al., 2004), a public domain image processing software, to determine the average grayscales for pore and grain. The boundary grayscale threshold was then determined as the average of the two average component (grains and pores) grayscales according to the standard approach of CT image processing in ASTM (1992). The individual pores were separated with the manual method in Blob3D in order to produce pore geometry data including maximum and minimum pore length, pore surface area, and pore volume. The resultant binary images were then imported to ImageJ for the reconstruction of 3D pore structure.

2.4. Mercury intrusion porosimetry

MIP is a widely-used technique for pore structure characterization, especially for the pore size analysis. It covers a larger detection range of pore size than XCT and it can accommodate larger

and thus more representative samples. Therefore, it can serve as a good reference for the evaluation of XCT-based results. Two Berea sandstone samples with a dimension of 1.5 cm × 1.5 cm × 1.5 cm were analyzed with mercury intrusion porosimetry (AutoPore IV 9500, Micromeritics, Norcross, GA). One of the cube samples was coated with epoxy on four sides to leave other two opposite sides as the principle intrusion direction. Pore structure parameters, including porosity, pore surface area, and bulk density were obtained from the intrusion data directly through the instrument software (AutoPore IV 9500 V1.09). For comparison the specific surface area was determined by N_2-adsorption (Nova 4000e, Quantachrome). PSD was deduced from the cumulative intrusion volume as discussed in Section 1, with the mercury surface tension of 485 dynes/cm and contact angle of 130°. A powdered Berea sandstone sample (<500 μm in particle size) was also measured with MIP to obtain the particle density.

3. Results and discussions

3.1. 2D X-ray images and 3D pore structures

Fig. 1 shows the 2D slices from the two XCT, with the scale bar differing by a factor of 10. The dark gray sections are pores, while the bright gray represents solid, most of which is quartz (accounting for ∼85% according to the X-ray diffraction (XRD) analysis by Baraka-Lokmanea et al. (2009)). The sparsely white spots are microcline or calcite (Baraka-Lokmanea et al., 2009). The low resolution image from μCT (Fig. 1a) presents a larger view of the sample with a diameter of 6.5 mm compared to the high-resolution synchrotron image (Fig. 1b) with the diameter of 0.72 mm. From the low resolution images, pores and mineral grains can be differentiated based on the grayscale; while for the high resolution images, more details can be observed for the pore structure. Although Berea sandstone is known as a uniform-textured porous material, certain extent of heterogeneity can still be observed in pore dimension scale of ∼1 mm (Fig. 1a). Two types of pores can be observed from Fig. 1b: interparticle and intraparticle pores, designated as type I and II, respectively in the figure. The interparticle pores were larger, with diameters of approximately 10–100 μm. The intraparticle pores, with diameters less than 10 μm, were developed in the outer boundary of the mineral grains and some of them are connected to the interparticle pores. Clay layers may contribute to the formation of the interparticle pores according to the SEM image, which is most likely kaolinite according to the XRD analysis by Baraka-Lokmanea et al. (2009). The boundary of the pores is more linear than curvy, which is characteristics for the shape of quartz grain. This is different from assumed spherical, ellipsoidal or cylindrical shapes used in many pore scale models.

The boundary threshold grayscale was set as 78 and 132 for images with low and high resolutions, respectively (more discussion on the threshold grayscale is presented in Section 3.2.1). Binary images based on the segmentation of the pores with the threshold grayscales were imported to ImageJ to generate 3D view of the pore structure (Fig. 2). The extracted pore structure is plotted in pink and green for the low and high resolution X-ray images, respectively. More details on pore structure can be observed in the high resolution images (Fig. 2b), including the large amount of intraparticle pores and the roughness of the pore surface; while the pore structure in low resolution (Fig. 2a) can be more representative with respect to porosity as will be discussed in Section 3.2.

3.2. Porosity

3.2.1. XCT results

In standard CT image processing practice, the proper threshold grayscale is the average of the two mean component grayscales (ASTM, 1992). The average grayscale for pores and grains is 62.5 and 93.8, respectively for X-ray μCT images obtained at a resolution of 12.7 μm. The threshold grayscale was thus set as 78. For the synchrotron XCT 0.35 μm images, the grayscale for pores and grains is 129.2 and 134.4, respectively. Therefore, threshold grayscale of 132 was applied to estimate the porosity. The resultant porosities are included in Table 1. Thresholding grayscale is important for determining the porosity from XCT images. Different image pre-processes and thresholding approaches can generate different results in porosity (e.g., Baveye et al., 2010). Nevertheless, the consistent pre-process and thresholding methods can assure the consistent comparison between different XCT resolutions in this study.

Conceptually, the porosity determined from the XCT images is the total porosity including both accessible and isolated pores. The actual smallest and largest pore lengths measured with Blob3D are found to be 16.1 μm and 425 μm by the low resolution XCT images, and 0.25 μm and 25 by the high resolution XCT. Therefore, the XCT-based porosity is actually the total porosity in the corresponding detecting pore size range (Table 1).

3.2.2. MIP results and comparison with XCT results

During MIP measurements, mercury is introduced to the pore spaces through connected paths under increasing pressures up to 60,000 psi, corresponding to a pore throat of 3 nm; therefore, the porosity measured with bulk rock sample is accessible (connected) porosity for pores >3 nm. The bulk sample without epoxy coating resulted in an accessible porosity of 23.1%, which is close to the calculated total porosity 23.2% based on the bulk density (2.03 g/cm^3) from the sample and particle density (2.64 g/cm^3) measured from the powder sample. This indicates that basically all the pores are
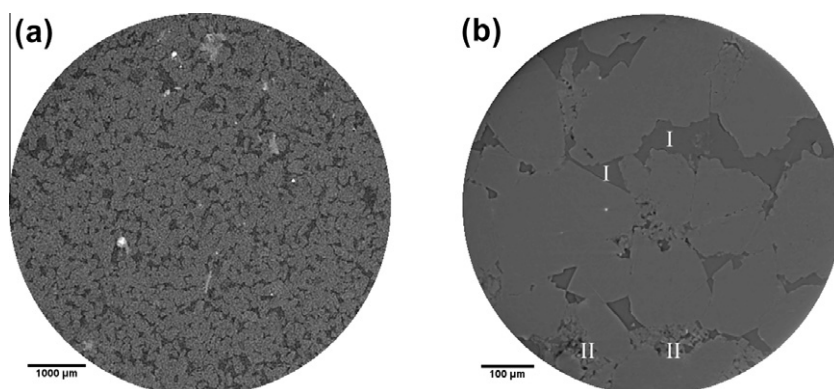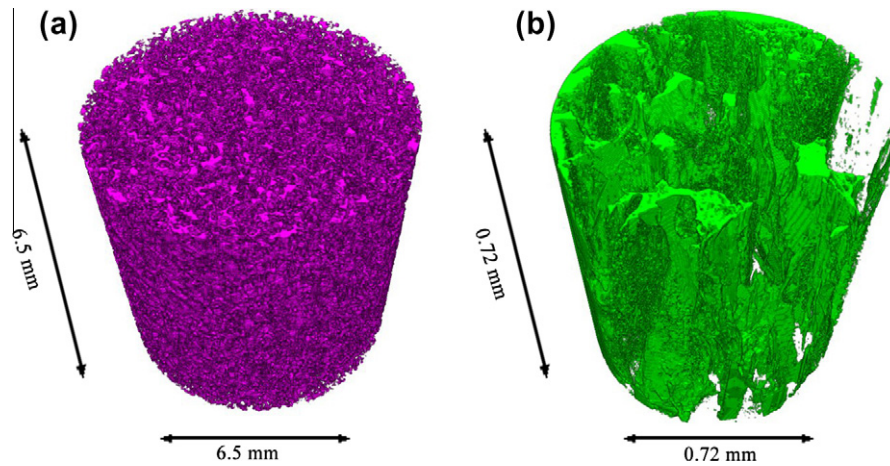

Fig. 1. Example 2D XCT images from resolution of (a) 12.7 μm and (b) 0.35 μm. Darker gray sections represent pores, bright gray denotes quartz grains, and white spots can be microclines or calcites. Intraparticle pores (Type I) and intraparticle pores (Type II) can be observed from the high resolution image (b).

Fig. 2. Reconstructed 3D pore structure from XCT images with resolution of 12.7 μm (a) and 0.35 μm (b). More details can be observed in the high resolution pore structure (b), such as large amount of smaller intraparticle pores and roughness of the pore surface; while pore structure in low resolution (b) can be more representative in porosity.

Table 1
Porosity, accessible fraction, and specific pore surface area obtained from MIP and XCT methods.

	MIP			X-ray 0.35 μm	X-ray 12.7 μm
	D^a > 0.003 μm	25 μm > D > 0.25 μm	D > 16.1 μm	25 μm > D > 0.25 μm	D > 16.1 μm
Total porosity	23.10%	16.64%[b]	15.95%[b]	19.4%	15.2%
Accessible fraction	85.0%	<85.0%	< 85.0%	98.4%	96.6%
Specific pore surface area (m²/g)	1.98	0.066[c]	0.009[c]	0.14	0.007

[a] D = Diameter.
[b] Calculated based on MIP PSD.
[c] Calculated based on MIP pore surface area vs. pore diameter.

within the connected pore clusters when all six faces of the cubic sample are open; therefore, the accessible porosity is equivalent to the total porosity in this case. On the other side, for the core plug sample (2.54 cm in diameter, 4 cm in height), measured helium porosity is 22.8%. This indicates consistent results from different methods.

Since MIP can detect pores with a minimum diameter of 3 nm, a much wider range than both XCT methods, it is expected that the total porosity from MIP (23.1%) is larger than the XCT-based porosities as shown in Table 1. However, to assess the accuracy of XCT method, it is more meaningful to compare the porosity in the corresponding detecting pore size range. Therefore, total porosities with pore diameter (D) of 25 μm > D > 0.25 μm and D > 16.1 μm, which are the detected pore size range for the two imaging methods, respectively, were calculated based on PSD of the uncoated sample from MIP to facilitate the comparison with the imaging methods (Table 1). More discussion on PSD will be presented in Section 3.3.

Porosity from low resolution XCT (15.2%) is found to be close to MIP-estimated porosity of pores with D > 16.1 μm (15.4%, Table 1). This indicates that the low resolution XCT can capture the porosity, specifically, the porosity of large pores (D > 16.1 μm). On the other side, porosity estimated from high resolution XCT (19.4%) is larger than MIP-estimated porosity of pores with 25 μm > D > 0.25 μm (16.6%). A potential reason can lie in the scale effect since the size difference (0.65 mm and 15 mm for high resolution XCT and MIP, respectively). Discussion in more detail on scale effect will be presented in Section 3.4.

3.3. Pore size distribution

Pore size distribution (PSD) from MIP method was derived from the cumulative mercury intrusion volume with stepwise increas-

ing pressures. PSD for the two bulk samples (coated and uncoated) are shown in Fig. 3; however, comparison of PSD with XCT-based results is based on PSD from uncoated sample as it included the overall pores. The incremental mercury intrusion volume at a given pressure corresponds to the pore throat permeable to mercury at this pressure and connected to the mercury percolation cluster. This will lead to a deviation from the PSD in a "real" geometric sense. Furthermore, the pore diameter from MIP refers to the pore throat diameter, which is different from PSD from the imaging method where the minimum length of the fitted ellipsoid enclosing the pore is taken as the pore diameter (see more details below). This will induce the inconsistency of the PSD results from the two methods.

PSD from the XCT images is supposed to reflect the "real" pore geometry as XCT images include both connected and isolated
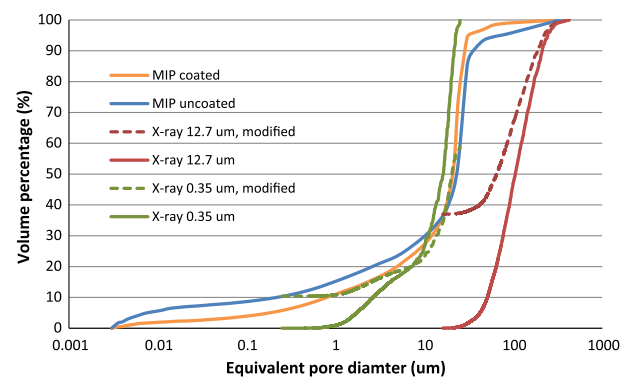
Fig. 3. Pore size distribution from MIP and XCT methods. In MIP, pore diameter refers to pore throat diameter; while it is the minor pore length of the best-fitted ellipsoid in the imaging method.

pores; however, because of the resolution limitation, the PSD from this method must be limited too. Another issue is the technical difficulty encountered in separating the pores. It is difficult for Blob3D to separate adjoining pores with no obvious geometric connecting throat. For these non-separated pores, no pore length can be measured. Consequently, only 32% and 78% (volume) of the total pores were separated and were used in the PSD analysis for the low and high resolution XCT, respectively. In image processing with Blob3D, a best-fit ellipsoid is calculated to fit the boundary of an object as closely as possible. The shortest length of the ellipsoid is taken as the pore diameter herein. Obviously, PSD from the low resolution XCT overestimates the overall pore size (Fig. 4) because it only allows for pores with $D > 16.1$ μm. The PSD was modified by assuming the fraction of $D < 16.1$ μm can be estimated based on the MIP PSD; however, the resultant PSD was still not close to the MIP PSD, specifically, the low resolution XCT overestimates the pore size (Fig. 3).

On the other hand, PSD from the high resolution XCT is in the comparable range with the MIP PSD (Fig. 3) although they cover different pore diameter ranges. For example, D_{50} from XCT PSD is 16.4 μm, while it is 20.0 μm from MIP PSD. The pore range fraction modified XCT PSD based on the same method mentioned above is closer to MIP PSD. As discussed above, the PSD from these two methods is expected to be different. Nevertheless, the XCT method with resolution of 0.35 μm generated comparable PSD with MIP for the pores in the range of 25 μm < D < 0.25 μm, which indicates the reliability of the high resolution XCT with respect to PSD determination.

3.4. Pore connectivity and scale effect for porosity and pore connectivity

Pore connectivity is another critical property of the pore structure which defines how well the pores are connected and therefore will affect the local fluid flow. Accessible fraction is used to express the pore connectivity in this paper. A burning algorithm in the code Percolate (Bentz and Garboczi, 1992), which counts the pores accessible from the surface in a way like "burning", was applied to the 3D binary XCT images to determine the accessible fraction. The burning algorithm searches neighbors in direct contact. The accessible fraction of 96.6% was obtained from the low resolution XCT images, while a slightly higher accessible fraction of 98.4% was obtained from the high resolution XCT images (Table 1). On the other side, for MIP method, a cube sample with epoxy coating in four faces results in accessible porosity in one principle direction, which was measured as 19.6%. The accessible fraction of

porosity in one principal direction can thus be calculated as the ratio of accessible porosity in one direction and the total porosity, which is 85.0%, assuming pores <3 nm are negligible for Berea sandstone. Again, to make more meaningful comparison, accessible fraction from MIP at the two corresponding detecting pore size ranges should be used for the comparison with XCT-based results. However, these data cannot be calculated without knowing the specific location of each pore, while they must be smaller than the overall accessible fraction of 85%. Comparison in Table 1 of accessible fractions shows clearly that XCT based results are larger than MIP-based results. This can be caused by two reasons: (1) the low resolution XCT overestimates the pore size, consequently, it may overestimate the pore connectivity by taking two disconnected smaller pores as one larger pore; and (2) scale effect exists for pore connectivity, as indicated by Ewing and Horton (2002) that the pore connectivity was higher at smaller scale.

To investigate the scale effect on total porosity and accessible fraction, four different scales of "cores" were extracted from the low resolution 3D structure with both core diameter and height of 0.72 mm, 1.4 mm, 2.8 mm, and 5.6 mm. Porosity and accessible fraction were determined for each cores and plotted in Fig. 3, along with the results from MIP. Observation of Fig. 4 reveals that the porosity from the low resolution X-ray images fluctuates for cores with a diameter <2.8 mm and tends to be stable between 15% and 16% for larger core diameter, which is in line with the MIP total porosity with $D > 16.1$ μm. This indicates that the scale effect does exist for porosity, specifically the large pore porosity ($D > 16.1$ μm). A volume with diameter and height of 2.8 mm can be taken as a representative element volume (REV) of the Berea sandstone for the large pore porosity. Sampling dimension smaller than the REV can result in either overestimation or underestimation of porosity. Similarly, the accessible fraction of pores larger than 16.1 μm from the low resolution XCT method also shows fluctuation for cores with a diameter <2.8 mm and tends to be stable at around 96.5% for cores with a larger diameter, which also indicates the existence of scale effect on pore connectivity. However, the change of accessible fraction between the gap between the sample size of 6.5 mm and 15 mm is not clear. It is worthy to note that the representative volume of other macroscopic parameters has not been evaluated, such as bulk density and surface area, for which the scale effect can be different (Baveye et al., 2002); therefore, the theoretical REV with diameter and height of 2.8 mm is specific to large-pore porosity and probably for pore connectivity herein.

3.5. Pore surface area

Pore surface area is an important influencing factor for the surface interaction and sorption. The specific surface area measured by N_2-BET is 0.985 m²/g, which can be underestimated due to the existence of oil film in the sample (French et al., 1995). The total pore surface areas obtained from the MIP and XCT method are listed in Table 1. Fig. 5 shows the relationship between pore surface area and pore diameter. The MIP method generated the largest total surface area of 1.98 m²/g. Specific surface area estimated with XCT images was calculated as the measured total surface area with Blob3D divided by the sample mass, which was in turn calculated as the volume times the bulk density of 2.02 g/cm³. There may be certain scale effects on bulk density which will result in different specific surface area. However, the value of 0.14 m²/g and 0.007 m²/g, estimated from the high- and low-resolution XCT images, respectively, are orders-magnitude smaller than the MIP-generated value. This indicates the significance of small pores in the pore surface area for Berea sandstone. As shown in Table 2, D_{50} of MIP pore surface area is 0.0045 μm, which accounts for only 1% of the total pore volume. On the other hand, D_{50} of the low resolution XCT generated pore surface area is 105 μm, which accounts
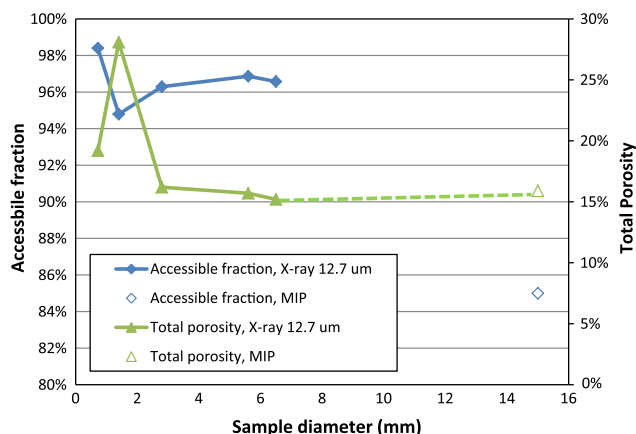

Fig. 4. Total porosity and accessible fraction from different sample core diameter extracted from low-resolution XCT images, along with the results from MIP.
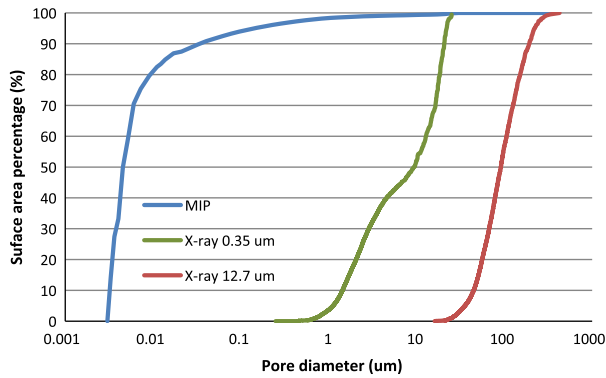
Fig. 5. Pore surface area vs. pore diameter obtained from MIP and the two XCT.

Table 2

D_{50} for cumulative pore surface area and the corresponding pore volume fraction from MIP and XCT methods.

	MIP	X-ray 0.35 μm	X-ray 12.7 μm
Pore surface area D_{50} (μm)	0.0045	9.6	105.0
Pore volume fraction	1.0%	29.0%	50.6%

for 50.6% of the pore volume. This indicates that for porous media with exclusively large pores, (e.g., $D > 16.1$ μm), the significance of smaller pores' effect on the surface area is similar to the larger ones.

There are inherent differences between the pore surface area calculations with MIP and image method. In MIP, pore surface area, A, is calculated by assuming a cylindrical shape of the pores, that is, $A = D/4V$, where V is the pore volume with pore diameter D. Using Blob3D for CT images, pore surface area is calculated based on the isosurface surrounding the object voxels. Therefore, the pore surface area will be slightly overestimated due to roughness induced by pixilation in the image method (Ketcham, 2005); while it will be underestimated due to the simplifying assumption of cylindrical pore shape in MIP. The MIP total pore areas in the range of the detection limit of each XCT method were also estimated (Table 1) based on the MIP-generated pore surface area distribution. Comparison of the pore surface area in the section of large pores ($D > 16.1$ μm), as lower limit detected by low resolution XCT) indicates similar results from the two methods (0.009 m^2/g vs. 0.007 m^2/g). This indicates that, for large pores, the assumed cylindrical pores can be satisfactory in the sense of surface area calculation. On the other hand, in the smaller pore section (25.0 μm > D > 0.25 μm), the XCT method generated larger surface area (0.14 m^2/g) than the MIP method (0.066 m^2/g). This indicates the simplified pore shape may lead to underestimation of the surface area. This point can be better understood with the discussion of hydraulic radius below.

3.6. Hydraulic radius

Hydraulic radius (R_h) is defined as the ratio of pore volume to pore surface area (V/A), which is equivalent to the perimeter over area (PoA) in 2D image analysis, based on which the individual core conductance and subsequently permeability can be estimated (Lock et al., 2002). R_h for each pore diameter is plotted in Fig. 6. Consistent with the assumption of cylindrical pore shapes in MIP calculation, R_h from MIP can be described by $D/4$. Values of R_h from the two XCT methods show a consistent trend in a power law form equation and are smaller than the MIP R_h, while the deviation is decreasing with an increasing pore diameter. This can be attributed to the slightly overestimated pore volume by image process-
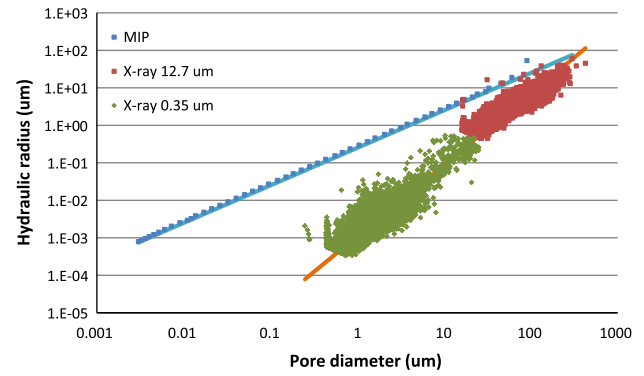

Fig. 6. Hydraulic radius (R_h) from MIP and the two XCT methods. MIP $R_h = D/4$ with R^2 of 0.999; R_h from the two XCT methods has consistent trend and can be described by $R_h = 0.0011D^{1.91}$ with $R^2 = 0.976$.

ing in Blob3D and the underestimation of pore surface area by MIP method, with the extent of underestimation decreases with an increasing pore diameter.

3.7. Aspect ratio

The aspect ratio is the major axis length divided by the minor axis length of the best-fit ellipsoid to the individual pore. Aspect ratio is one of the important geometric parameters, which can affect the permeability, the transverse hydraulic dispersion, and the tortuosity. High aspect ratio provides more grain to grain contact, thus decreasing the pore compressibility (Saleh and Castagna, 2004). In the MIP method, pore throat to pore cavity ratio can be obtained, but conceptually it is different from the aspect ratio and hence not compared herein. Fig. 7 shows the aspect ratio frequency from the two XCT methods. Basically, both of them display similar distribution of aspect ratio, spanning from 1 to 16, with aspect ratio of 3 dominating, which accounts for more than 40% for both resolutions. This indicates less compaction extent in the Berea sandstone and thus indicates relatively high permeability.

3.8. Discussion on resolution effect of XCT and its implication on resolution selection

A critical issue on the XCT method is to obtain the "realistic" physically representative pore structure, and resolution is the key. According to the MIP measurement, ~35% of the pores in the Berea sandstone sample have a diameter smaller than 12.7 μm. This can be the reason behind the fact that images with low resolution of 12.7 μm contain substantial ambiguous zones
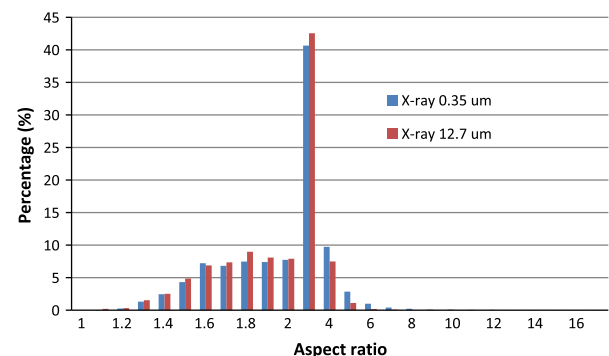

Fig. 7. Aspect ratio from the two XCT analyses. Both resolutions generated similar results with aspect ratio of 3 dominated.

in which the precise differentiation of pores and grains is difficult, as shown in the discussion in Section 3.1. Nevertheless, the low resolution XCT can still capture the large-pore porosity ($D > 16.1$ μm); however, it overestimates the pore size and pore connectivity. On the other hand, the high resolution image of 0.35 μm (pores with diameter smaller than the resolution account for ~6.7% of the total pore volume according to MIP measured pore size distribution of uncoated sample) can basically be thresholded with greater certainty and can capture the pore size distribution more accurately (Fig. 3). However, the field of view is small and the detecting pore size range is narrower, thus will not be representative regarding to porosity and pore connectivity of larger samples. Other property and flow process can be expected to be more representative in larger volume, too. Resolution effect can also be seen in specific surface area; however, both low and high resolution generated better results in pore surface area than MIP, especially for smaller pores. They also generated consistent results in hydraulic radius and aspect ratio.

Porosity, pore size distribution, and pore connectivity are the key parameters which define the pore geometry and topology; therefore, the resolution effect of XCT on these parameters is critical in the results. As indicated by the discussion above, both low and high resolution XCT can generate misleading results of either less accurate or less representative. Therefore, the selection of resolution must be a compromise between the accuracy and representativeness. Specifically, for the Berea sandstone used in this study, using the TOMCAT beamline, a resolution of 1.85 μm with a corresponding field of view of 3.7 mm^2 may generate images of the best quality in both regards of accuracy and porosity representativeness. The field of view of 3.7 mm^2 is larger than the REV for porosity of 2.8 mm^2, and the pores with diameter smaller than 1.85 μm accounts for ~13.5% of the total pore volume.

Another important aspect of accuracy and representativeness is that they are specific for different research objectives. For example, in scenarios of gas or non-aqueous phase liquid (NAPL) flow in natural rocks which is under partially saturated condition and thus smaller pores are occupied by water, the pore structure generated with relatively low resolution can still be valid as long as it adequately represents the larger pores where the non-wetting phase flow actually occurs. On the contrary, this relatively low resolution will not be adequate when water flow or multi-phase flow needs to be considered. Another example is linking pore structure parameter to different transport parameters, such as diffusivity and permeability. Diffusion will occur in both small and large pores, actually even faster in small pores for gas due to Knudsen flow effect, while larger pores contribute predominantly to permeability over smaller pores. Therefore, for the same rock sample, the resolution selected for diffusion analysis should be higher than that for the permeability analysis.

4. Conclusions

In this paper, Berea sandstone was examined with two XCT of two resolutions of 0.35 μm and 12.7 μm to evaluate the resolution effect. In addition, the results from the imaging method were compared quantitatively with that from MIP method to evaluate the resolution effect further. Direct visualization of 3D pore structures is realized where different aspects of details such as pore type, pore surface area, and pore geometry can be observed. Key parameters of the pore structure are discussed in a more quantitative manner.

High resolution images can reveal more details of the pore structure and were more accurate in describing of porosity and pore size, while the field of view was limited and thus result in non-representative results. By contrast, low resolution images provided larger field of view and were able to capture the large-pore

porosity ($D > 16.1$ μm), while they overestimated the pore size and pore connectivity. Scale effect is found in respect to porosity and pore connectivity estimation from the imaging methods. A value of REV for large-pore porosity and probably for large-pore connectivity with diameter and height of 2.8 mm is obtained for the Berea sandstone sample. On the other hand, both low- and high-resolution XCT generated better results in surface area, especially for smaller pores. They also generated consistently smaller hydraulic radii. A power-law-form equation can describe the hydraulic radius obtained from the two XCT methods. In addition, similar aspect ratio is also obtained from the two resolution XCT methods.

The results from XCT image analysis on porosity, pore size distribution, and pore connectivity indicate that both low and high resolution XCT can generate misleading result in pore structure and consequently the fluid flow inside. Therefore, the selection of a proper resolution is critical and should be based on the pore size distribution of the rock sample of interest and the specific purpose of the investigation in order to produce the best quality in respect of both accuracy and representativeness. At least, the limitations of the resolution on the pore structure parameters, especially porosity, pore size distribution, and pore connectivity should be realized when they cannot be overcome. On the other hand, the ultimate solution may lie in how to obtain the representative (or larger) images while with consistent accuracy. Further research is required for this purpose.

Acknowledgments

References

Abramoff, M.D., Magelhaes, P.J., Ram, S.J., 2004. Image processing with ImageJ. Biophoton. Int. 11 (7), 36–42.

American Petroleum Institute Recommended Practice (API RP) 40 (1960), Recommended Practice for Core Analysis Procedure (1st Ed.). Am. Petrol. Inst., Dallas, Texas.

Amirtharaj, E.S., Ioannidis, M.A., Parker, B., Tsakiroglou, C.D., 2011. Statistical synthesis of imaging and porosimetry data for the characterization of microstructure and transport properties of sandstones. Transport Porous Med. 86, 135–154.

ASTM (American Society for Testing and Materials), 1992. Standard guide for computed tomography (CT) imaging, ASTM designation E 1441–92a, in 1992 annual book of ASTM standards, section 3 metals test methods and analytical procedures: Philadelphia, ASTM, pp. 690–713.

Baraka-Lokmanea, S., Mainc, I.G., Ngwenyac, B.T., Elphick, S.C., 2009. Application of complementary methods for more robust characterization of sandstone cores. Mar. Pet. Geol. 26, 39–56.

Barret, E.P., Joyner, L.G., Halenda, P.P., 1951. The determination of pore volume and area distributions in porous substances. I. Computations from nitrogen isotherms. J. Am. Chem. Soc. 73, 373–380.

Baveye, P., Rogasik, H., Wendroth, O., Onasch, I., Crawford, J.W., 2002. Effect of sampling volume on the measurement of soil physical properties: simulation with X-ray tomography data. Meas. Sci. Technol. 13, 775–784.

Baveye, P.C., Laba, M., Otten, W., Bouckaert, L., Sterpaio, P.D., Goswami, R.R., Grinev, D., Hu, Y., Liu, J., Mooney, S., Pajor, R., Sleutel, S., Tarquis, A., Wang, W., Wei, Q., Sezgin, M., 2010. Observer-dependent variability of the thresholding step in the quantitative analysis of soil images and X-ray microtomography data. Geoderma 157, 51–63.

Bentz, D.P., Garboczi, E.J., 1992. Modeling the leaching of calcium hydroxide from cement paste: effects of pore space percolation and diffusivity. Mater. Struct. 25, 523–533.

Bera, B., Mitra, S.K., Vick, D., 2011. Understanding the micro structure of Berea Sandstone by the simultaneous use of micro-computed tomography (micro-CT) and focused ion beam-scanning electron microscopy (FIB-SEM). Micron 42, 412–418.

Bhattad, P., Willson, C.S., Thompson, K.E., 2010. Segmentation of low-contrast three-phase X-ray tomography images of porous media. In: Alshibli, K.A., Reed, A.H., (Eds.). Advances in Computed Tomography for Geomaterials, pp. 254–261. ISTE, London; Willey, Hoboken, NJ, USA.

Blunt, M., King, M.J., Scher, H., 1992. Simulation and theory of 2-phase flow in porous-media. Phys. Rev. A 46 (12), 7680–7699.

Brusseau, M.L., Peng, S., Schnaar, G., Costanza-Robinson, M.S., 2006. Relationships among air-water interfacial area, capillary pressure, and water saturation for a sandy porous medium. Water Resour. Res. 42, W03501.

Bryant, S., Mellor, D., Cade, C., 1993. Physically representative network models of transport in porous media. Aiche J. 39 (3), 387–396.

Chen, Q., Song, Y.Q., 2002. What is the shape of pores in natural rocks? J. Chem. Phys. 116 (19), 8247–8250.

Diamond, S., Leeman, M.E., 1995. Pore size distributions in hardened cement paste by SEM image analysis. Mater. Res. Soc. Symp. Proc. 370, 217–226.

Dong, H., Blunt, M.J., 2009. Pore-network extraction from micro-computerized-tomography images. Phys. Rev. E 80, 036307.

Dufresne, T., Chemielewski, P., Borah, B., Laib, A., 2004. Encyclopedia of Biomaterials and Biomedical Engineering. Bowlin, G.L., Wnek, G. (Eds.). Informa Healthcare.

Ewing, R.P., Horton, R., 2002. Diffusion in sparsely connected porespaces: temporal and spatial scaling. Water Resour. Res. 38 (12), 1285. http://dx.doi.org/10.1029/2002WR001412.

Fredrich, J.T., Digiovanni, A.A., Noble, D.R., 2006. Predicting macroscopic transport properties using microscopic image data. Journal of Geophysics Research 111(B3), B03201 (Solid Earth).

French, P.R., Mannhardt, K., De Bree, N., Shaw, J.C., 1995. Assessment of solvent extraction efficiency in sandstones using BET specific surface area measurements. J. Can. Pet. Technol. 34 (3). http://dx.doi.org/10.2118/95-03-03.

Gladkikh, M., Bryant, S., 2005. Prediction of imbibition in unconsolidated granular materials. J. Colloid Interface Sci. 288 (2), 526–539.

Hilpert, M., McBride, J.F., Miller, C.T., 2000. Investigation of the residual-funicular nonwetting-phase-saturation relation. Adv. Water Resour. 24 (2), 157–177.

Holzer, L., Cantoni, M., 2011. Review of FIB-tomography. In: Russell, P., Utke, I., Moshkalev, S. (Eds.). Nanofabrication using focused ion and electron beams. Oxford University Press, NY, USA, ISBN 9780199734214.

Ioannidis, M.A., Kwiecien, M.J., Chatzis, I., 1996. Statistical analysis of the porous microstructure as a method for estimating reservoir permeability. J. Petrol. Sci. Eng. 16, 251–261.

Keller, L.M., Holzer, L., Wepf, R., Gasser, P., 2011. 3D geometry and topology of pore pathways in Opalinus clay: implications for mass transport. Appl. Clay Sci. 52, 85–95.

Ketcham, R.A., 2005. Computational methods for quantitative analysis of three-dimensional features in geological specimens. Geosphere 1, 32–41.

Kittler, J., Illingworth, J., 1986. Minimum error thresholding. Pattern Recogn. 19, 41–47.

Lindquist, W.B., Lee, S.M., Coker, D.A., Jones K.W., Spanne P., 1996. Medial axis analysis of void structure in three-dimensional tomographic images of porous media. J. Geophys. Res. 101(B4), pp. 8297–8310 (Solid Earth).

Lock, P.A., Jing, X., Zimmerman, R.W., 2002. Predicting the permeability of sandstone from image analysis of pore structure. J. Appl. Phys. 92 (10), 6311–6319.

Munchw, B., Holzer, L., 2008. Contradicting geometrical concepts in pore size analysis attained with electron microscopy and mercury intrusion. J. Am. Ceram. Soc. 91 (12), 4059–4067.

Murray, K.L., Seaton, N.A., Day, M.A., 1999. Use of mercury intrusion data, combined with nitrogen adsorption measurements, as a probe of pore network connectivity. Langmuir 15, 8155–8160.

Otsu, N., 1979. Threshold selection method from grey-level histograms. IEEE Trans. Syst. Man Cyb. 9, 62–66.

Prodanovic, M., Lindquist, W.B., Seright, R.S., 2007. 3D image-based characterization of fluid displacement in a Berea core. Adv. Water Resour. 30 (2), 214–226.

Saleh, A.A., Castagna, J.P., 2004. Revisiting the Wyllie time average equation in the case of near-spherical pores. Geophysics 69, 45–55. http://dx.doi.org/10.1190/1.1649374.

Seaton, N.A., Walton, J.P.R.B., Quirke, N., 1989. A new analysis method for the determination of the pore size distribution of porous carbons from nitrogen adsorption measurements. Carbon 27, 853–867.

Stampanoni, M., Groso, A., Isenegger, A., Mikuljan, G., Chen, Q., Bertrand, A., Henein, S., Betemps, R., Frommherz, U., Böhler, P., Meister, D., Lange, M., Abela, R., 2006. Trends in synchrotron-based tomographic imaging: the SLS experience. Developments in X-Ray Tomography V, edited by Ulrich Bonse, Proc. of SPIE Vol. 6318, 63180M, 1605–7422/06, doi: 10.1117/12.679497.

Washburn, E.W., 1951. Note on a method of determining the distribution of pore sizes in a porous materials. Proc. Natl. Acad. Soc. 7, 115–116.

Webb, P.A., 2001. An introduction to the physical characterization of materials by mercury intrusion porosimetry with emphasis on reduction and presentation of experimental data. Volume and Density for Particle Technologists. Micromeritics Instrument.

Wildenschild, D., Hopmans, J.W., Vaz, C.M.P., Rivers, M.L., Rikard, D., 2002. Using X-ray computed tomography in hydrology: systems, resolutions, and limitations. J. Hydrol. 267 (3–4), 285–297.

Ye, G., 2003. The microstructure and permeability of cementitious materials. Delft University Press, Delft, the Netherlands. pp. 82–3.